

Original Article

Sustainable synthesis of bivalent Ni²⁺, Co²⁺, and Cu²⁺ Schiff base complexes *via* ball milling as a green approach: A study of spectroscopic characterization, cyclic voltammetry, bioactivity, DFT analysis, SAR, drug likeness, and molecular docking

Khlood Saad A. Abou-Melha*

Department of Chemistry, Faculty of Science, King Khalid University, Abha 62529, Saudi Arabia

ARTICLE INFO

Keywords:

Benzothiazol derivatives and its complexes
Binding affinity
Bioactivity assessment
Cyclic voltammetry
Green chemistry

ABSTRACT

The synthesis of 3-(2-hydroxybenzylidene)-N-(benzothiazol-2-yl)hydrazine-3-oxopropanamide (H₂BT) presents a novel approach to chelation by the incorporation of carbonyl and benzothiazole groups, which significantly enhances binding efficiency and selectivity toward transition metal ions such as Ni²⁺, Co²⁺, and Cu²⁺. This work uniquely employs a ball milling technique for the formation of Schiff base solid chelates, positioning it as a more environmentally friendly alternative to conventional solvent-based methods. A comprehensive characterization of the synthesized compounds was conducted using various analytical techniques, including thermal analyses (TG, DTG), elemental analyses (¹H, ¹³C-NMR Infrared (FTIR), electron spin resonance (ESR), UV-visible, Energy dispersive X-ray (EDX), powder X-ray diffraction (XRD), Mass spectra (MS)), and Scan electron microscope (SEM), validating the structural integrity and composition of the ligand and its metal complexes. Additionally, quantum-mechanical investigations employing density functional theory (DFT) provide insights into the electronic properties of the prepared compounds. The bioactivity of H₂BT and its metal chelates was systematically evaluated using standard assays and assessing cytotoxicity, antioxidant activity, antibacterial effects, DNA-binding capacity, and erythrocyte hemolysis. The binding affinities of the complexes were further analyzed using the Molecular Operating Environment (MOE) software, referencing the crystallographic structure of the BCL2 receptor-bound ligand (PDB: 2w3l). To elucidate the complexation behavior in solution, cyclic voltammetry was performed at 291.15 K with copper (II) ions in a Dimethyl sulfoxide (DMSO)-water mixture, revealing critical electrochemical insights. Overall, this study not only enriches the understanding of H₂BT as a ligand but also highlights its potential applications in bioinorganic chemistry, drug development, and catalysis, underscoring the innovation in utilizing a green synthesis approach for metal coordination chemistry.

1. Introduction

The target of this work is the preparation of a new derivative of Schiff base of N-(benzothiazol-2-yl)-3-(2-hydroxybenzylidene)hydrazinyl-3-oxopropanamide according to the history of this family in the biological field. Their significance is evident in various areas, such as coordination chemistry, where they are essential for the creation of metal complexes with transition metals, particularly Ni²⁺, Co²⁺, and Cu²⁺. Due to their increased stability and bioactivity, these chelates are useful in materials science, electrochemistry, and catalysis, among other areas. Moreover, Schiff bases are being thoroughly studied for drug development due to their wide range of biological activities, including antibacterial, antifungal, and anticancer qualities. Their capacity to interact with biological targets highlights their potential as medicinal substances [1-3].

Furthermore, in chemical synthesis, Schiff bases are crucial intermediates that enable the synthesis of more complicated compounds. Agrochemicals and dyes are among the many organic compounds that are created because of their transformation and reactivity. Schiff bases also play a key role in metabolic pathways and enzyme processes [4].

They play a part in important biological functions such the creation of several metabolic intermediates and collagen cross-linking. Lastly, the versatility of Schiff bases makes them valuable for a variety of fields, in both industry and research [5]. Their capacity to unite material science and organic chemistry demonstrates their revolutionary potential in both basic and applied science.

Nickel (II) is an essential transition metal for several key enzymes, notably urease, which hydrolyzes urea into ammonia and carbon dioxide, a crucial reaction in nitrogen metabolism. It also plays a role in hydrogenases involved in energy production in some microorganisms. Additionally, nickel ions regulate gene expression, and imbalances can lead to various biological disorders [6,7]. Also, cobalt (II) is an important transition metal with diverse applications. In medicine, it is vital for vitamin B12, DNA, and red blood cell formation. Cobalt compounds are studied for their antibacterial properties and used as industrial catalysts. Additionally, cobalt enhances the performance of electronic devices in optoelectronics and plays a role in radiopharmaceuticals for medical imaging and therapy [8,9]. Moreover, Copper (II) ions are significant in coordination chemistry and biological systems, serving as essential cofactors in enzymes like cytochrome c oxidase for cellular respiration,

*Corresponding author:

E-mail address: dr.khlood@hotmail.com (K.S.A. Abou-Melha)

Received: 20 January, 2025 Accepted: 18 March, 2025 Epub Ahead of Print: 15 May 2025 Published: 21 May 2025

DOI: 10.25259/AJC.56_2025

superoxide dismutase for antioxidant defense, and tyrosinase for melanin biosynthesis [10,11]. Additionally, copper (II) chelates are widely used as catalysts in organic reactions, including polymerization and oxidation, and have various industrial applications in chemical production and pharmaceutical synthesis, highlighting their versatility and importance [12].

As a green chemistry technique, ball milling is used to prepare Ni^{2+} , Co^{2+} , and Cu^{2+} divalent chelates with the novel Schiff base (H_2BT), an eco-friendly substitute for conventional solvents [13-15]. By improving mixing and increasing the contact between reactants, ball milling produces more complete reactions, which greatly increases the yield and efficiency of Schiff base complex synthesis. By removing the requirement for solvents and frequently cutting reaction times when compared to conventional techniques, this mechanochemical approach further reduces its environmental impact [16]. Several well-used methods were used to illustrate the likely coordination and binding characteristics of solid chelates. Also, in recent years, Density Functional Theory (DFT) has emerged as a pivotal tool in computational chemistry, enabling researchers to predict and analyze the electronic structures and properties of various compounds with high accuracy. The application of DFT analysis allows for the investigation of molecular interactions, stability, and reactivity, serving as a significant complement to experimental methods [17,18]. So, in this study, some key parameters such as molecular geometries, electronic distribution, and energy profiles were calculated, which provided valuable insights into the fundamental behavior of compounds under study. Specifically, in the context of our research on benzothiazole derivatives functionalized frameworks. DFT study was performed not only to elucidate the relationships between their structural features and biological activity but also help rationalize experimental observations with theoretical predictions. Additionally, the bioactivity of H_2BT and its metal complexes, including their antibacterial, antioxidant, cytotoxic, erythrocyte hemolysis, and DNA-binding properties, were examined using standard methods to evaluate their inhibitory effect. Lastly, the Molecular Operating Environment module (MOE) has been used to confirm the level of inhibition of the produced compounds.

2. Materials and Methods

2.1. Preparation of ligand and its Ni^{2+} , Co^{2+} , and Cu^{2+} metal chelates

3-(2-hydroxybenzylidene)-N-(benzothiazol-2-yl)hydrazine-3-oxopropanamide were refluxed for 3 hrs in absolute ethanolic solution (95%) to create pure H_2BT , as Scheme 1S illustrates. Solid chelates of the acetate salts of Ni^{2+} , Co^{2+} , and Cu^{2+} were synthesized using the high-energy ball milling approach, which shortens the reaction time (20 mins) and yields a pure compound with a high yield of about 98% (Scheme 1). This approach adheres to sustainability ideals by minimizing the usage of dangerous chemicals and consuming less energy. Additional purification was done by recrystallization using absolute ethanol.

2.2. Equipment

Scheme 2S shows every total of apparatus accustomed the suggested geometries of the prepared compounds.

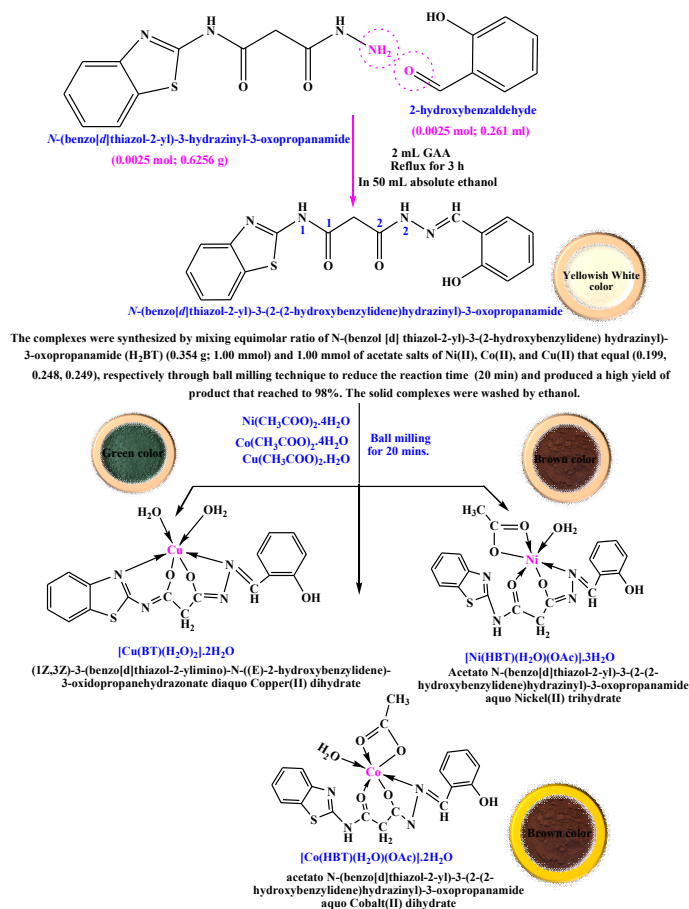
2.3. Theoretical calculation

Utilizing DMOL3 and the Materials Studio package, the theoretical conclusions were made [19,20]. The geometry optimization of the resulting compounds was verified by using DFT, utilizing the Lee-Yang-Parr non-local correlation functional (B3LYP) [21].

2.4. Evaluation of biological activity

2.4.1. Investigation of antimicrobial activity

Using Ampicillin and Coltrimazole as standards the proportion of activity index for microorganisms, for instance *Escherichia coli* (gram negative), *Bacillus subtilis* (gram positive) bacteria, and *Candida albicans*



Scheme 1. The outline synthesis of solid complexes. Scheme 1S, the synthesis of the ligand, Scheme 2S, the images of the instruments used.

via the disk diffusion procedure (Scheme 3S), reflected the level of activity in the specified time span and geographic region [22-24].

2.4.2. Investigation of antioxidant activity

The produced materials' antioxidant capability was measured using the 2, 2-azino-bis (3-ethylbenzothiazoline-6-sulfonic acid (ABTS) procedure at 734 nm. Scheme 4S explained that the decrease in color intensity is known as the inhibition percentage [25].

2.4.3. Investigation of DNA binding

The ability of transcription factors to interact with DNA in neutral media at 630 nm and pH 7 was assessed using the DNA-binding colorimetric assay, which has been depicted in Scheme 5S [26].

2.4.4. Investigation of 3-(4,5-dimethylthiazol-2-yl)-2,5-diphenyltetrazolium bromide (MTT) cytotoxic

The MTT test (Tetrazolium Bromide) is a colorimetric technique that uses MCF-7 and HEPG-2 cell lines to quantify cellular metabolic activity as a gauge of cell viability, proliferation, and indirect cytotoxicity of the chemicals being synthesized. The resulting absorbance is measured at 570 nm, as in Scheme 6S [27,28].

2.4.5. Investigation of Erythrocyte hemolysis

Hemolysis is defined as the destruction of erythrocytes, or red blood cells, which are an essential component of blood. Using ascorbic acid as the positive control, antioxidants have taken this check into consideration for preventing the damage that free radicals cause to erythrocyte membranes. Scheme 7S provided a spectrophotometric explanation of the hemolysis grade for the examined materials at 540 nm [29].

2.5. Molecular docking calculations

Using the AD4/MGLTools-1.5.7 software suite on the Windows platform, a computational molecular docking analysis was performed to elucidate and evaluate the binding empathies of the investigated complexes with the energetic site of the *BCL2* gene [30,31]. This was accomplished by using the AD 4 program in combination with the Lamarckian Genetic Algorithm (LGA) to evaluate the compounds' binding affinities for the indicated biomolecules. The protein-ligand rigid-flexible docking process was conducted using the Lamarckian Genetic Algorithm (LGA) with the following parameters: 27,000 generations, a maximum of 250,000 energy estimations, and alteration and border rates of 0.02 and 0.8, correspondingly. This assay comprised multiple procedure such as grid building, ligand and protein manufacturing, and selection. The crystallographic structure of the ligand-attached BCL2 receptor (PDB: 2w3l) was discovered using the RCSB protein database (PDB database) [32]. The original structure was brought into the visualizer, and then water molecules, heteroatoms, chain B, and any remaining atoms were eliminated. Next, the active site linked to the co-crystallized DRO ligand was found [33]. Within the BCL2 exploration domain, a 35 x 35 x 35 Å grid box with 0.375 Å grid spacing was used. We utilized the x, y, and z coordinates of 40.91, 27.92, and -10.02, respectively.

2.6. Cyclic voltammetry

Three primary electrodes were employed to construct the electrochemical cell that we used in our experiments:

- Using 3M KCl as a reference electrode and Ag/AgCl.
- A functional electrode was the glassy carbon.
- Platinum wire served as the auxiliary.
- As a supporting electrolyte, 30 mL of HCl (0.1 M) solution was added to each electrode. The US convention provided CV data once the DY 2100 potentiostat was connected.

3. Results and Discussion

3.1. The isolation of complexes

The results detailing the physical properties and elemental analysis of H_2BT , along with the synthesized chelates, have been presented in Table 1. Both the chemical compositions and the proposed formulas were examined through the comparison of practical and calculated percentages derived from the analysis. The melting points of the synthesized complexes exceeded 300°C, indicating their stability. These complexes were formed in a 1:1 molar ratio (metal to ligand). The prepared ligand displayed solubility in hot absolute ethanol, whereas the isolated solid complexes were soluble in dimethyl sulfoxide (DMSO) and dimethylformamide (DMF).

3.2. $^{13}C/^1H$ NMR analysis

Figure 1S displayed the H_2BT ligand 1H and ^{13}C NMR analysis spectra, which were obtained in Dimethyl sulfoxide (DOMS). The 1H NMR

spectrum showed three signals at 11.56, 12.56, and 11.035 ppm, which were identified as originating from the protons (OH), (NH₁), and (NH₂), respectively. A strong signal at 3.62 ppm was identified as coming from the protons (CH₂). Additionally, multiplet signals of aromatic protons were found in the 6.56–8.27 ppm area, with the (N=C—H) signal appearing at 8.45 ppm. Additionally, Table 1S displayed the coupling constant that was determined for each doublet and triplet signal.

The (C=O)₁ as well as (C=O)₂ were identified by two signals at 166.913 and 166.407 ppm in the ^{13}C NMR spectra for H_2BT , (C=N)_{azo} & (C=N)_{thiazol} were identified by two signals at 157.880, 168.00 ppm, and (C—OH) was identified by a signal at 162.067 ppm [34].

3.3. Mass spectra

The molecular ion peak [M]⁺ at m/z = (20.84%) in the ligand's mass spectrum corresponded to the ligand moiety [(C₁₇H₁₄N₄O₃S) atomic mass 487.13 U] and was equal to its molecular weight. Additionally, a base peak that matched the target H_2BT primary fragmentation molecular weight was seen at m/z = 5 7.09. The different molecular ion peaks that appeared in the H_2BT mass spectrum (abundance variety 2-100%) were associated with ligand fragmentation, which was caused by the breaking of several bonds within the molecule through successive degradation that led to many essential peaks because of the production of many radicals (Scheme 8S).

3.4. Infra-red spectra

Table 1 was provided an explanation of the physical parameters and elemental analysis data for H_2BT in addition to its manufactured chelates. Following their correlation, the chemical compositions and the proposed formula were both examined using experimental and computed percentages.

The vibrational bands seen at 1690, 1657, 3448, 2927, 3214, 3187, 1605, and 1624 cm⁻¹ in the infrared spectra of H_2BT (Figure 2S) were attributed to (C = O)₁, (C = O)₂, (O - H), (CH₂), (N - H)₁, (N - H)₂, (C = N)_{azo}, then (C = N)_{thiazol}, correspondingly, as shown in Table 2S [35].

In IR spectrum of [Cu(BT)(H₂O)₂] complex, H_2BT functioned as a binegative tetradentate ligand via the two deprotonated enolized carbonyl oxygens (=C- O₁) & (=C- O₂), and two nitrogen's groups (C=N)_{azo} & (C=N)_{thiazol} [36]. This mode of coordination was supported by: (i) The shift of vibrations of both nitrogen's groups (C=N)_{azo} & (C=N)_{thiazol} to lower wave numbers; (ii) The disappearance of both (C=O)₁ & (C=O)₂ with parallel appearance for new vibrational bands at 1202 cm⁻¹ and 1153 cm⁻¹, which are attributed to (C - O)_{1(enolic)} & (C - O)_{2(enolic)}; (iii) The disappearance of (NH)₁ & (NH)₂ with new bands appearing at 1637 cm⁻¹ and 1632 cm⁻¹ which are attributed to (C = N*)₁ & (C=N*)₂; and (iv) The appearance of new vibrations at 511 & 485 cm⁻¹, which may be related to (Cu - O) & (Cu - N), respectively.

Also, in IR spectra of [Co(HBT)(H₂O)(OAc)].2H₂O and [Ni(HBT)(H₂O)(OAc)].3H₂O chelates, the H_2BT acted as a mononegative tridentate via (C = N)_{azo}, (C = O)₁, and (=C- O-)₂ groups [36]. This mode of complexation was suggested based on the following observations: (i) The (C=N)_{azo} as well as (C=N)_{thiazol} bands shift to lower wave number numbers; (ii) The (C=O)₂ and (NH)₂ bands disappearance with

Table 1. Physical properties and elemental analyses for H_2BT and its complexes.

No.	Compounds Empirical formula F.W.: Formula weight Found (Calculate)	Physical properties		Yield %	Elemental analyses % (Calcd.) Found				
		Color	M.P. (°C)		%C	%H	%S	%N	Metal %
1	H_2BT C ₁₇ H ₁₄ N ₄ O ₃ S 354.13 (354.38)	Yellowish-white	234	78	(57.66) 57.62	(3.98) 4.03	(9.05) 9.11	(15.81) 15.94	-
2	[Cu(L)(H ₂ O) ₂].2H ₂ O CuC ₁₇ H ₂₀ N ₄ O ₇ S 487.96 (487.36)	Green	> 300	98	(41.84) 41.45	(4.13) 3.86	(6.56) 6.82	(11.48) 11.92	(13.02) 13.52
3	[Co(HBT)(H ₂ O)(OAc)].2H ₂ O CoC ₁₉ H ₂₂ N ₄ O ₈ S (525.06)	Brown	> 300	98	(43.31) 43.35	4.2 (4.17)	(6.12) 6.09	10.64 (10.67)	(11.15) 11.19
4	[Ni(HBT)(H ₂ O)(OAc)].3H ₂ O NiC ₁₉ H ₂₄ N ₄ O ₉ S (543.175)	Brown	> 300	96	(41.88) 41.93	(44.48) 44.45	(5.91) 5.89	(10.22) 10.29	(10.72) 10.78

analogous appearance of novel vibrations at (1635, 1605) and (1153, 1155) cm^{-1} that are assigned to $(\text{C}=\text{N}^*)_2$ & $(\text{C}-\text{O})_2$ [37]; (iii) Novel vibrational bands appeared at (505, 580) & (464, 476) cm^{-1} that may be movable to $(\text{M}-\text{O})$ & $(\text{M}-\text{N})$, correspondingly; (iv) The appearance of new vibrations at (1471, 1469) & (1346, 1377) which related to $\nu_s(\text{O}-\text{C}-\text{O})$ and $\nu_{as}(\text{O}-\text{C}-\text{O})$, respectively indicated the bidentate manner of acetate groups.

3.5. UV-visible and magnetic moment

As shown in Table 3S and Figure 3S, the results indicate that the prepared complexes of Ni^{2+} and Co^{2+} possessed octahedral geometry, whereas the Cu^{2+} complex exhibited deformed octahedral geometry [37].

The electronic spectrum of an octahedral Ni^{2+} complex showed two bands at 17241 and 27027 assignable to ${}^3\text{A}_2 \rightarrow {}^3\text{T}_{1g}$ (F) & ${}^3\text{A}_{2g} \rightarrow {}^3\text{T}_{1g}$ (P) transitions, correspondingly. Also, the calculated values of ($D_q=1104$), ($B=736$), ($\beta=0.758$) & ($\nu_2/\nu_1=1.55$) confirmed the proposed octahedral structure. In addition to, the value of the magnetic moment (3.12 B.M.) can be considered additional evidence for an octahedral geometry.

The electronic spectrum of the octahedral Co^{2+} complex displayed two bands at 14815 cm^{-1} and 19802 cm^{-1} ascribed to ${}^4\text{T}_{1g} \rightarrow {}^4\text{A}_{2g}$ (F) & ${}^4\text{T}_{1g} \rightarrow {}^4\text{T}_{1g}$ (P) transitions, correspondingly. Also, the calculated values of ($D_q=793$), ($B=933$), ($\beta=0.961$) & ($\nu_2/\nu_1=2.15$) suggested an octahedral structure. Furthermore, octahedral geometry around the Co(II) ion was confirmed by the value of the magnetic moment (5.12 B.M.). In the electronic spectrum of Cu^{2+} , the complex showed a broad band at 16129 cm^{-1} with a shoulder at 14388 cm^{-1} , which are assigned to ${}^2\text{B}_{1g} \rightarrow {}^2\text{E}_g$ and ${}^2\text{E}_g \rightarrow {}^2\text{A}_{1g}$ transitions, correspondingly, in a tetragonally distorted octahedral configuration. Also, the octahedral geometry around the Cu(II) ion was confirmed by the magnetic moment value (2.03 B.M.).

3.6. Electron spin resonance

The room-temperature solid state ESR spectrum (Figure 4S) of $[\text{Cu}(\text{BT})(\text{H}_2\text{O})_2]$ complex exhibited axially symmetric g-tensor parameters with " $g_{||} > g_{\perp} > 2.0023$ ", indicating that the copper site had a dx^2-y^2 ground-state characteristic of tetragonally distorted octahedral stereochemistry [38]. Moreover, in the Cu^{2+} complex, there was no band related to the forbidden magnetic dipolar transition at half-field (*ca.* 1500 G, $g = 4.0$); this suggested that there was no Cu-Cu interaction, and thus, the Cu^{2+} complex was mononuclear [39]. The exchange interaction between Cu^{2+} centers in the solid complex in the axial symmetry was expressed in Eq. (1) as follows:

$$G = (g_{||} - 2) / (g_{\perp} - 2) = 4 \quad (1)$$

As suggested by Hathaway [40], if $G > 4$, there is an exchange contact between the Cu^{2+} centers; if $G < 4$, there is a significant exchange interaction in the solid complex. The G value of 4.60 is the calculated value. Also, the f factor ($g_{||}/A_{||}$) was calculated from the ESR spectrum to measure the extent of distortion of the copper (II) complex which equal to 138, which indicated the existence of important dihedral angle distortion in the xy -plane and a typical deformed octahedral structure surrounding the copper site. Additionally, Eqs. (2) & (3) [41] were used to determine the molecular orbital coefficients, such as α^2 that measures the covalency in-plane β -bonding between a copper 3d orbital and the ligand orbitals and β^2 that measures the covalency in-plane π -bonding:

$$\alpha^2 = (A_{||} / 0.036) + (g_{||} - 2.0023) + 3 / 7(g_{\perp} - 2.0023) + 0.04 \quad (2)$$

$$\beta^2 = (g_{||} - 2.0023) E / -8\lambda\alpha^2 \text{ at } = -828 \text{ cm}^{-1} \quad (3)$$

Through strong in-plane π -bonding in the Cu^{2+} chelate, the magnitude of α^2 (0.80) and β^2 (0.77) showed that both in-plane σ -bonding and in-plane π -bonding are dependable and significantly covalent.

3.7. Thermal investigation

The investigated complex was thermally stable up to 30°C, as indicated by the Cu^{2+} complex's TG curve, after which the chelate began to dehydrate. The $2\text{H}_2\text{O}$ molecules were proposed to be outside the coordination sphere of the copper ion with a 3.57% weight loss over

the temperature range of 30-119°C, which is consistent with relatively low temperature [42]. Next, as shown by the Thermogravimetric (TG) curves (Table 4S and Figure 5S), the second temperature range (119-235)°C indicated the existence of $2\text{H}_2\text{O}$ inside the coordination sphere with an 8.04% weight loss. The organic moiety's thermal degradation began at 230°C. The elimination of the ligand's $\text{C}_6\text{H}_6\text{O}$, and $\text{C}_7\text{H}_5\text{NS}$ fragments may be the cause of the 48.88% weight loss seen in the TG curve during the temperature range of 235-587°C. Ultimately, the breakdown of the remaining organic moiety ($\text{C}_4\text{N}_3\text{O}$) accounted for 21.79% of the weight loss in the temperature range of 587-850°C. Copper oxide, which made up 16.92% of the initial mass of the chelate, was the final burned product.

Additionally, the $[\text{Co}(\text{HBT})(\text{H}_2\text{O})(\text{OAc})] \cdot 2\text{H}_2\text{O}$ TG curve. In the temperature range of 30-124°C, the Co(II) complex exhibited a 6.26% weight loss, which corresponded to two water molecules that were not coordinated (Table 4S and Figure 5S). One molecule each of coordinating water and acetic acid were linked to the weight loss in the temperature range of 124-257°C, with a weight loss of 15.37%. The obtained curves showed a 37.48% decrease in the temperature range of 257-447°C, which can be attributed to the presence of organic moieties ($\text{C}_6\text{H}_6\text{O}$, $\text{C}_4\text{N}_3\text{O}$). Lastly, the elimination of the remaining moiety of the organic molecule ($\text{C}_7\text{H}_5\text{NS}$) was responsible for the 26.61 percent weight loss in the temperature range of 447-800°C. Cobalt oxide (CoO) was the end product at 14.28% above 800°C.

3.8. EDX investigation

One analytical technique for determining the chemical makeup of a sample under investigation is EDX analysis. According to the spectra displayed in Figure 6S, the complex formation and the lack of impurities in the sample were confirmed by the complexes involving $\text{M} = (\text{Co}^{2+}, \text{Cu}^{2+}, \text{and Ni}^{2+})$, C, N, O, and S [34,43].

3.9. Scanning electron microscope (SEM) investigation

By using a concentrated electron beam to scan the surface, the SEM technique produces images of the materials under investigation (Co^{2+} , Cu^{2+} , and Ni^{2+}). The target sample's atoms and electrons then interact to produce a variety of signals that provide precise details about the sample's composition and surface topography. As shown in Figure 1, SEM was authorized to examine the complexes' surface geometry. The results showed that Cu^{2+} complexes with spherical grains in terms of relative crystallinity. However, the other pictures displayed a rocky appearance, which could be the result of large particles or amorphous samples [44,45].

3.10. X-ray diffraction investigation

A good non-destructive analytical technique for examining the composition, orientation, and phase crystal structure of solid, liquid, and powder materials is X-ray diffraction. As shown in Figure 7S, the Cu^{2+} chelate was examined at room temperature (RT) using (Cu, K α) radiation. The compound under examination had an amorphous character, as evidenced by the diffraction pattern, which was adjusted within the range of " $10^\circ < 2\theta < 90^\circ$ " [46].

3.11. Molecular chemical parameters

In chemistry and materials research, DFT is a powerful quantum computational mechanical modeling method that can be used to calculate a wide range of parameters of nearly any type of atomic system. Figure 2 displayed the optimal structure of H_2BT and its solid chelates, which were created in the gas phase. Furthermore, the dipole moment, binding energy, exchange-correlation energy, total energy, spin polarization energy, and electrostatic energy frontier atomic orbitals (E_{HOMO} , E_{LUMO}) [47] are some significant quantum parameters that could be evaluated and indicate the stability of the compound. These have been included in Table 2.

The following conclusions can be drawn from the results:

- As shown in Table 3 and Figure 3, the significant reliability of H_2BT and its metal chelates is demonstrated by the negative magnitude of the E_{HOMO} and E_{LUMO} energies.

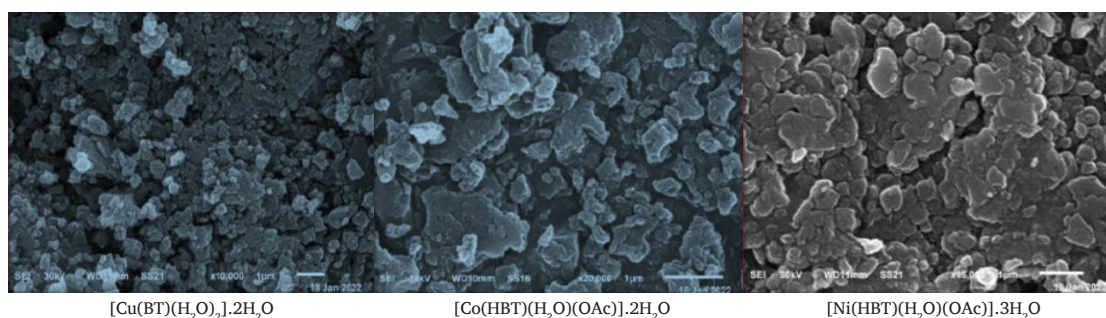


Figure 1(a-c). SEM of isolated solid complexes.

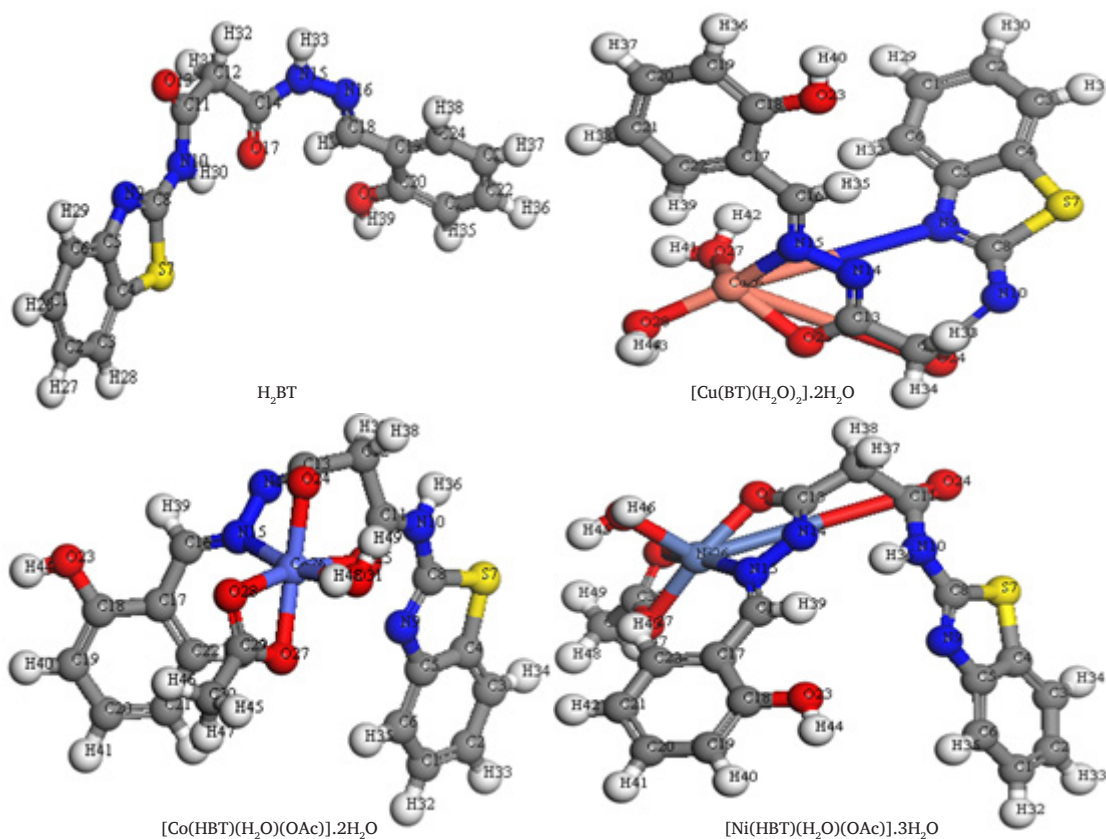


Figure 2. Optimized structure of isolated solid complexes.

Table 2. The molecular parameters of isolated solid compounds.

Compound	Total energy (Ha)	Binding energy (Ha)	Spin polarization energy (Ha)	Sum of atomic energies (Ha)	Exchange correlation energy (Ha)	Electrostatic energy (Ha)	Kinetic energy (Ha)	Dipole moment (debye)	HOMO (eV)	LUMO (eV)
1	-1512	-7.190	2.179	-1490	3.033	-0.447	-11.957	6.286	-5.615	-2.798
2	-1893	-7.819	2.311	-1862	3.321	-2.572	-10.869	20.545	-4.776	-2.769
3	-1962	-8.833	2.593	-1960	3.842	-5.701	-9.570	4.434	-4.624	-3.540
4	-1987	-8.887	2.569	-1987	3.815	-4.592	-10.679	12.581	-5.249	-4.475

ii. The lengthening of the bonds at the active sites of the free ligands that took part in coordination-prepared complexes (Table 5S & Figure 8S).

iii. As shown in Table 6S & Figure 9S, the shift in bond angles of prepared chelates suggested an octahedral geometry surrounding central metal ions with sp³d² or d²sp³ [48,49].

iv. Solid chelates have larger binding energy values than H₂BT, indicating greater stability for the produced chelates.

3.11.1. Molecular electrostatic map (MEP)

As shown in Figure 10S [50], MEPs for H₂BT and its separated chelates have three distinct zones based on their color. The blue area

Table 3. Calculated some quantum parameters for isolated solid complexes.

Compounds	1	2	3	4
Energy (eV)				
H	1.4073	1.0019	0.5429	0.3883
ω	8.8513	7.1213	8.3312	11.8266
μ	-4.2073	-3.7740	-4.0816	-4.8632
σ	0.7113	0.9979	1.8414	2.5739
χ	4.2074	3.7739	4.0819	4.8632
E _{HOMO}	-5.611	-4.774	-4.624	-5.250
E _{LUMO}	-2.812	-2.770	-3.537	-4.472
E _{Band gap}	2.815	2.002	1.084	0.774

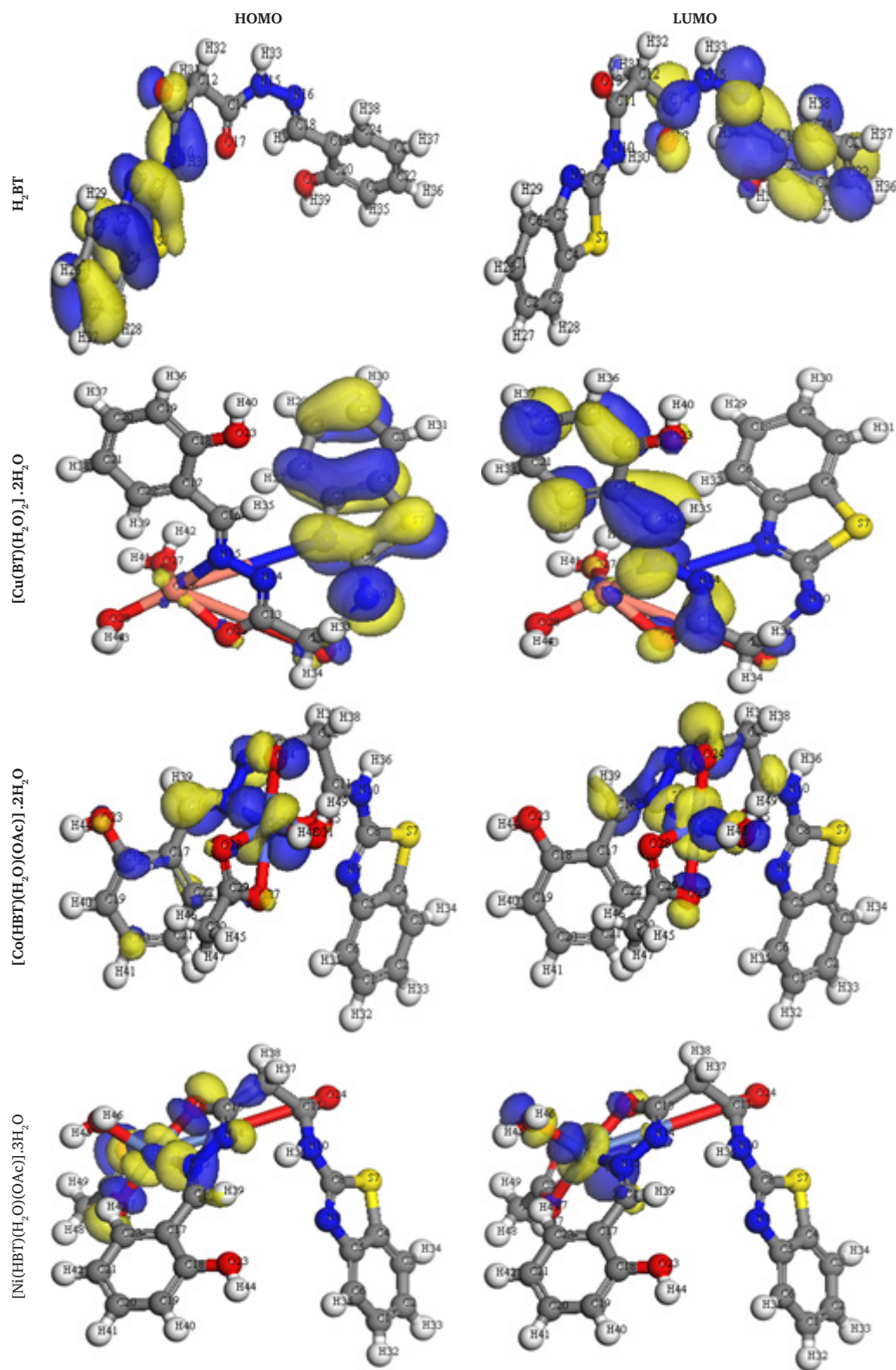


Figure 3. The HOMO and LUMO for isolated solid compounds. HOMO: Highest occupied molecular orbital, LUMO: Lowest unoccupied molecular orbital.

with repulsive potential represented low electron density related to nucleophilic attack areas, the green area represented zone with neutral electrostatic potential, and the red attractive potential area is

responsible for the electrophilic bout zone known with high electron density. MEP maps provide information about the target molecule's electron density supply.

This knowledge is essential for anticipating the locations of electrophilic and nucleophilic assaults, particularly for metal complexes. The researcher can recognize where and how reactions are expected to happen by viewing regions of high and low electrostatic potential. Furthermore, activities that establish the gratitude of one molecule by another, such as drug receptors and enzyme–substrate interactions, can be studied using the electrostatic potential.

3.12. Cyclic voltammetry technique

A versatile electrochemical technique, cyclic voltammetry (CV) is typically employed to examine the redox characteristics of Schiff bases. The following are the primary goals of using CV to Schiff base complexes, especially those containing transition metals like copper (II):

- To comprehend their electrochemical characteristics and possible uses for the target Schiff base, the CV approach was used.
- The CV approach sheds light on the reversibility of the redox processes, the stability of various oxidation states, and the mechanisms underlying electron transport. This can provide information about the ligand effects and coordination environment.
- For applications like fuel cells and sensors, CV aids in assessing their catalytic stability and efficiency.
- Comprehending the electrochemical characteristics of these complexes helps direct the creation of novel materials with specialized qualities for certain uses, such electrical or energy storage devices.

3.12.1. In case of copper (II)

By means of a supporting electrolyte (0.1 M KCl) in 50% DMSO-H₂O (V/V), a GC working electrode within the potential range (1.2 to -1.2 V), and a 0.1 V/s scan rate, the voltammetric work of Cu²⁺ solution was carried out at 291.15 K, as shown in Figure 4. Since the backward scan shows two anodic peaks the (Cu⁰/Cu¹⁺) first potential peak (E_{pa1}) at 0.321 V and the (Cu¹⁺/Cu²⁺) other peak (E_{pa2}) at - 0.102 V it is evident that the Cu²⁺ solution is electro-active. Two reduction peaks can be seen in the front scan: the first peak (E_{pc1}), which is (Cu²⁺/Cu¹⁺), appeared at -0.701V, and the second peak (E_{pc2}), which is (Cu¹⁺/Cu⁰), appeared at 0.058 V. Consequently, the following might be used to show the electrochemical mechanism:

The oxidation process: Cu⁰ → Cu⁺¹+e⁻ (0.321 V)

Cu⁺¹ → Cu⁺²+e⁻ (0.102 V)

The reduction process: Cu⁺²+e⁻ → Cu⁺¹ (-0.701 V)

Cu⁺¹+e⁻ → Cu⁰ (0.058 V)

Randles-Sevcik was used to determine the peak current (I_p) [51,52]. Additionally, Eqs. (4,5) [53] were used to evaluate the difference in potential (ΔE_p):

$$I_p = 0.4463nFAC (nFvD / RT)^{1/2} \quad (4)$$

n: Number of transferred electrons

C: Molar concentration in mol/L

I_p: Current in ampere

v: Scan rate in volts/s

D: Diffusion coefficient of redox particles in cm²/s

A: Electrode surface area in cm²

$$\Delta E_p = E_{p,a} - E_{p,c} \quad (5)$$

Numerous significant factors (Q, α_{na}, & ks) can be calculated using the previously discovered values (I_p, E_{pc}, & E_{pa}). Eq. (6) can be used to compute the redox ions of surface concentration [54].

$$\Gamma = ip4RT / n2 F2 A v \quad (6)$$

F: The Faraday constant that equal 96485.33 C/mol

n: The e- numbers in redox reactions

R: The gas constant that equal 8.314 J/mol.K

T: Temperature in Kelvin

Eq. (7) has been used to estimate the charge transfer coefficient "α"
[55]:

$$\alpha na = 1.857 RT / (E_{pc} - E_{pa} / 2) \quad (7)$$

Eq. (8) [56] has been used to evaluate the charge quantity consumption in the electrochemical processes:

$$Q = NFA \quad (8)$$

Eq. (9) can be used to determine the heterogeneous charge transfer rate constant "ks":

$$ks = 2.18 [Dc \alpha na F v / RT]^{1/2} \exp[\alpha 2nF \Delta E_p / RT] \quad (9)$$

As shown in Table 7S, the components that were taken into consideration (Dc, T, R, F, n, ΔE_p, α_{na}, & v) were computed for both the cathodic and anodic peaks. Additionally, as the CuCl₂ concentration rose, most of the desired components increased, favoring the occurrence of diffusion [57].

3.12.2. CV of Cu²⁺ in the existence of H₂BT

Using Glassy carbon electrodes (GCE) with a potential range of -1.2 - 1.2 V, the interaction redox behavior of CuCl₂ with H₂BT, as shown in Figure 4, was investigated in a KCl 0.1 M solution in a mixed solvent

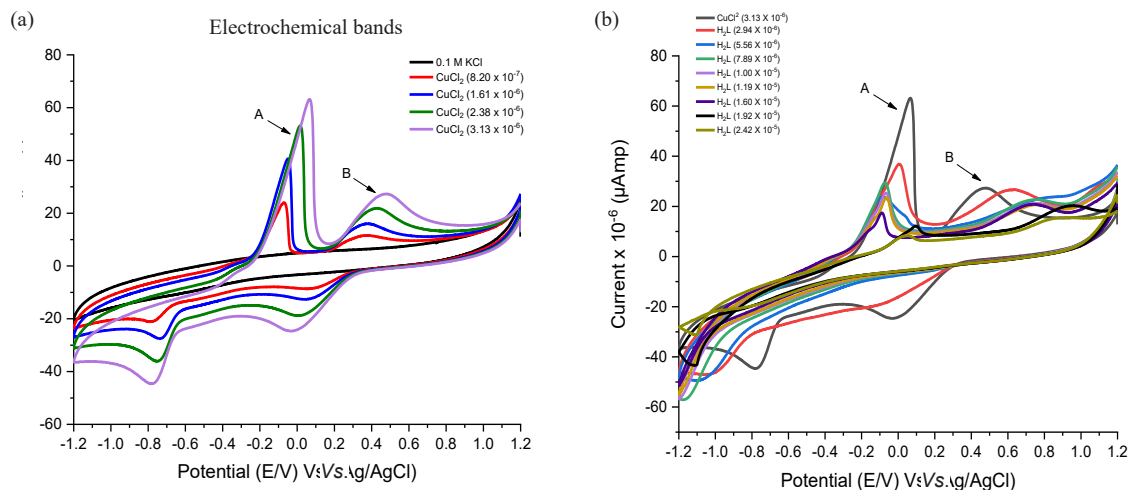


Figure 4. The cyclic voltammogram of CuCl₂ in (a) Absenteeism and (b) Existence of varying concentrations of ligand at 291.15 K. Electrochemical bands: A,B

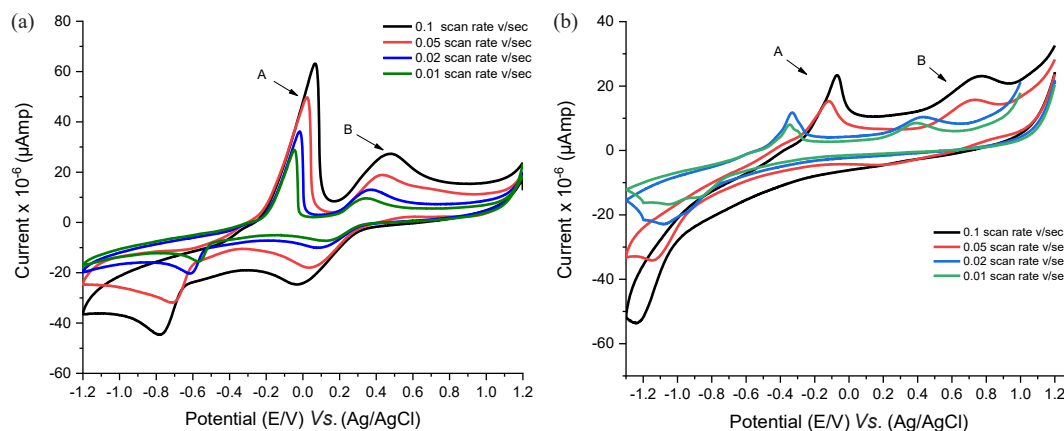


Figure 5. The cyclic voltammogram of CuCl_2 at various scan rates in (a) absenteeism and (b) presence of H_2BT at 291.15 K. Electrochemical bands: A,B

of DMSO and water. The achieved current peaks have dropped as the concentration of H_2BT has increased, favoring the covalency between H_2BT and the copper ions. Additionally, there has been a shift in the anodic and cathodic potential peaks, indicating substantial physical contact between H_2BT and copper. Changes in the computed magnitudes of E_s° , k_s , E_{pc} , E_{pa} , ΔE_p , i_{pa} , i_{pc} , Q , α_{na} , & Γ coincided with changes in the voltammogram shape as shown in Table 8S.

3.12.3. Effect of scan rate on Cu- H_2BT complex

The voltammograms obtained for Cu^{2+} , both in the absence and presence of H_2BT at 291.15 K in 0.1 M KCl, have been presented in Figure 5, showcasing various scan rates (0.01, 0.02, 0.05, and 0.1 V/sec). The data revealed the following observations:

- The peak current increased linearly with the scan rate.
- The cathodic and anodic peak positions shifted toward negative and positive potentials, respectively.

These findings were supported by the linear relationship between the peak currents and the scan rates, as illustrated in Figure 6, which suggests a diffusion-controlled redox mechanism. The ratio of the current peaks was greater than 1, indicating the system's quasi-reversibility. The solvation and kinetic data for Cu^{2+} at various scan rates, both in the presence and absence of H_2BT , have been detailed in Tables 9S and 10S.

3.12.4. Stability constants and Gibbs free energies for Cu- H_2BT complex at 291.15 K

As shown in Tables 11S and 12S, it was observed that the Gibbs free energies (ΔG) and stability constants (β_{Mx}) of the physical interactions

between the prepared ligand H_2BT and the copper ions increased with higher concentrations of H_2BT . The effect of the scan rate, detailed in Table 9S, 10S, revealed that most of the parameters (Γ_c , Γ_a , Q_c , and Q_a) decreased as the scan rate decreased, indicating a preference for stronger complexation.

3.13. Biological examines

3.13.1. Antimicrobial investigation

The discussion on the outcomes of the activity index for H_2BT and its metal chelates is crucial for a comprehensive understanding of their antibacterial and antifungal properties, especially in comparison to standard antibiotics such as Ampicillin and antifungal agents like Colitrimazole. Here, we can expand upon several key aspects of the findings, focusing on their implications and contextual importance in the field of medicinal chemistry and microbiology [58].

3.13.1.1. Comparative analysis of activity index values

The moderate activity observed for H_2BT and its metal chelates relative to Ampicillin suggests that while these compounds exhibit some level of antibacterial effectiveness, their efficacy may not yet match that of established antibiotics. This pointed to the potential for further optimization of H_2BT or its chelates to enhance their antibacterial properties.

3.13.1.2. Specific bacterial strains and activity levels

Notably, the lower activity values for the metal chelates against *B. subtilis* and *E. coli* could indicate selective sensitivity or resistance patterns that warrant in-depth investigations. This trend raises questions

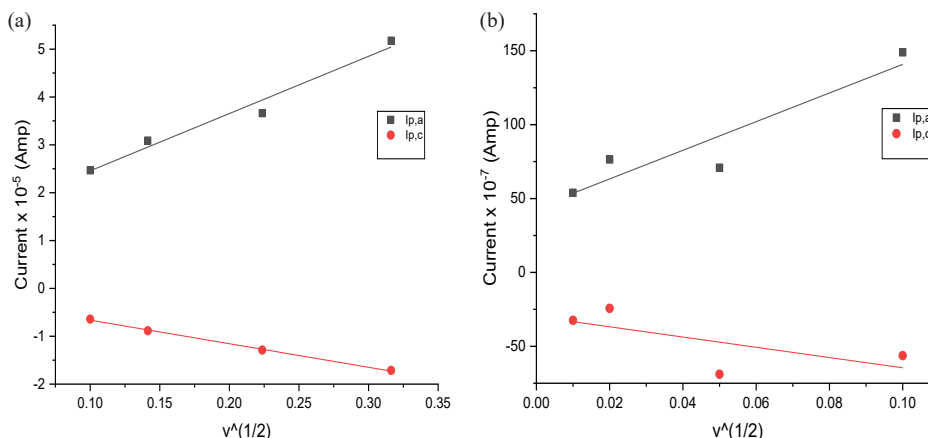


Figure 6. Relation (i_p vs. $v^{1/2}$) for CuCl_2 at final adding in (a) absenteeism and (b) presences of H_2BT K for wave (A).

about the mechanisms of action and how these compounds interact with specific bacterial targets. Understanding the biological pathways affected by these chelates could provide insights into their antibacterial mechanism and still pave the way for designing compounds that overcome existing resistance.

3.13.1.3. Highlighting the ni complex

The [Ni(HBT)(H₂O)(OAc)].3H₂O complex generally showed the highest percentage activity among the tested chelates, signifying that nickel coordination could enhance the bioactivity of H₂BT. This observation warrants further exploration of metal ion influence on the pharmacodynamics of the ligand. For instance, research into coordination chemistry might elucidate why nickel enhances activity, possibly due to improved solubility, stability, or affinity for microbial targets.

3.13.1.4. Antifungal activity observations

With respect to antifungal activity, the finding that H₂BT exhibits moderate values against *Candida albicans* in comparison to Clotrimazole aligns with current trends in exploring novel antifungal agents as resistance to conventional treatments rises. Again, the performance of the metal chelates against fungal targets and the superior activity of the nickel complex could reflect a similar enhancement mechanism. So, further studies should be focused on understanding the interactions between these chelates and fungal cell membranes or metabolic pathways.

3.13.1.5. Future directions for research

The results from Table 13S and Figure 7 provide a solid foundation for potential future research avenues. Investigating the broader spectrum of metal complexes involving other transition metals or varying ligand structures could lead to novel discoveries in the quest for new antibacterial and anti-fungal agents. Moreover, conducting *in vivo* studies could bridge the gap between empirical laboratory findings and practical therapeutic applications.

3.13.1.6. Conclusion

In summary, while the reported activity indices of H₂BT and its metal chelates demonstrate moderate effectiveness against bacterial and fungal strains, the distinctions observed, particularly the prominence of the [Ni(HBT)(H₂O)(OAc)].3H₂O complex, suggest areas ripe for exploration [59]. A deeper understanding of these mechanisms and their biological implications could lead to more effective applications in combating microbial resistance. The value of % activity index was estimated through Eq. (10):

$$\% \text{ Activity Index} = \frac{\text{inhibitory zone for test compound, diameter}}{\text{inhibitory zone for standard, diameter}} \times 100 \quad (10)$$

3.13.2. Antioxidant investigation

The L-ascorbic acid, a common antioxidant, is used to evaluate the antioxidant rank of the generated Schiff base compounds using the ABTS colorimetric assay, which is recognized as illustrated in Figure 8 [60]. According to the experimental results shown in Table 14S, the ligand (H₂BT) and the standard ascorbic acid showed values that were roughly comparable, while all of the complexes that were tested had lower antioxidant values that were comparable to those of the standard ascorbic acid (88.50%) and the ligand (H₂BT) (85.70%) while [Co(HBT)(H₂O)(OAc)].2H₂O Out of all the substances examined, showed the highest activity index (40.60%).

DFT outcomes data can provide valuable insights into the antioxidant properties of Schiff base compounds by elucidating the electronic structures and reactivity patterns of the molecules involved. Specifically, DFT calculations can help identify the active sites on the ligand and metal complexes that are responsible for their antioxidant activity.

The relationship between DFT studies and antioxidant activity can be further understood through the following points:

1. A lower HOMO-LUMO gap generally indicated a higher reactivity, which may correlate with enhanced antioxidant properties.
2. Also, by computing the energy changes involved in these reactions, we can predict how effectively a compound can donate electrons or hydrogen atoms to neutralize free radicals.
3. Moreover, correlating DFT-derived properties (like binding energies or reaction pathways) with experimental results from assays like the ABTS colorimetric assay can help clarify why certain complexes exhibit higher or lower antioxidant capacities.

3.13.3. DNA-binding

Doxorubicin was used as a positive control to estimate the right concentration at which primary absorbance for DNA/methyl green solution (IC₅₀) saw a 50% decline, resulting in a complete lack of methyl green absorbance (Table 4). The findings showed that the metal chelates, notably [Co(HBT)(H₂O)(OAc)].2H₂O, had the greatest IC₅₀ values (82.52±2.90), whereas H₂BT had moderate values. Doxorubicin's positive control showed an IC50 value of 31.54±1.50, indicating a high binding affinity to DNA [61,62].

3.13.4. Cytotoxicity assay

To determine the value of sample concentrations that result in 50% of cells dying (IC₅₀), cytotoxicity was calculated using doxorubicin as a standard medication, as shown in Table 4 [63]. Eq. (11) was utilized to get the relative cell viability percentage.

$$\text{Average cell viability} = \frac{A570 \text{ of treated samples}}{A570 \text{ of untreated sample}} \times 100 \quad (11)$$

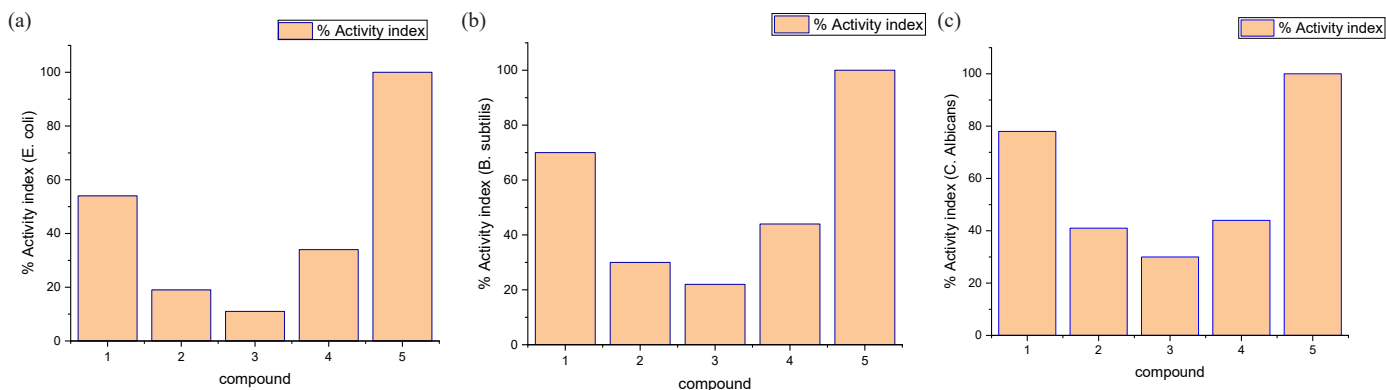


Figure 7. (a-c) Antimicrobial results in terms of % activity index of (1) H₂BT, (2) [Cu(BT)(H₂O)₂].2H₂O, (3) [Co(HBT)(H₂O)(OAc)].2H₂O, (4) [Ni(HBT)(H₂O)(OAc)].3H₂O, and (5) standard drugs (Clotrimazole in case of fungi & Ampicillin in case of bacteria) .

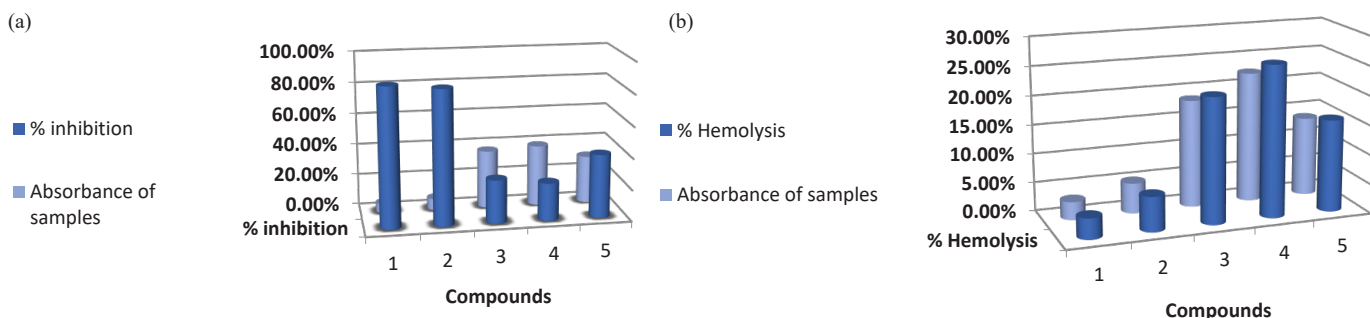


Figure 8. Antioxidant activity of (1) Ascorbic acid, (2) H₂BT, (3) [Cu(BT)(H₂O)₂].2H₂O, (4) [Co(HBT)(H₂O)(OAc)].2H₂O, (5) [Ni(HBT)(H₂O)(OAc)].3H₂O compounds. (a) The ABTS colorimetric examine using ascorbic acid as standard (b) The Erythrocyte hemolysis using Ascorbic acid as standard.

Table 4. DNA/methyl green colorimetric test for cytotoxicity and DNA binding to human tumor cells.

Method	A		B
	In vitro Cytotoxicity IC ₅₀ (μg)*		DNA-active compound
Compound	HePG2	MCF-7	DNA/methyl green (IC ₅₀ μg/mL)
DOX	4.51±0.2	4.17±0.2	31.56±1.5
1	6.03±0.4	8.17±0.5	33.64±1.7
2	47.12±2.5	36.97±2.4	63.45±2.7
3	64.54±3.2	51.54±3.1	82.53±3.1
4	25.21±1.8	29.10±2.2	56.92±2.4

*IC₅₀ (μg/mL): very strong (1 – 10), strong (11 – 20), moderate (21 – 50), weak (51 – 100) and non-cytotoxic > 100.

Cytotoxic chemicals are those that have a higher IC₅₀ than DOX and can decrease the viability of tumor cells (HePG2, MCF-7). The H₂BT ligand data showed the highest cytotoxicity, measuring 8.17 ± 0.60 magnitudes for MCF-7 and 6.02 ± 0.40 magnitudes for HEPG-2. However, the cytotoxicity value of the Co²⁺ complex was modest, but that of the Cu²⁺ and Ni²⁺ complexes was significant.

3.13.5. Erythrocyte hemolysis

Eq. (12), where (A) is the sample absorbance at 540 nm and (B) is the supernatant absorbance at identical wavelengths induced after centrifugation, was used to calculate the percentage of erythrocyte hemolysis.

$$(A/B) \times 100 \% \quad (12)$$

All of the studied compounds showed strong hemolysis activity values when compared to Vit-C as the standard, where the [Co(HBT)(H₂O)(OAc)].2H₂O, as indicated by the practical results displayed in Table 14S. The greatest absorbance value (0.225) and hemolysis percentage (26.10%) were found in the Co(II) complex [64,65].

3.14. Molecular docking

The BCL2 family proteins, which are essential for either promoting or preventing apoptosis, have been the subject of much research over the past ten years. Their crucial role in controlling apoptosis, carcinogenesis, and reactions to anticancer therapies is the reason for this increased interest [66]. By blocking its anti-apoptotic action, many tiny compounds known as BCL2 inhibitors increase the vulnerability of cancer cells to apoptosis. These inhibitors work by attaching themselves to the groove of the protein and preventing it from doing its job [67]. To assess the modalities of drugs, the degree of their binding, and their interactions with a particular BCL2 inhibitor, this study used a comparative molecular docking analysis. The best docking positions were examined, along with the interactions of metal and ligand complexes with the 2w3l receptor. The medication was used

as a standard reference for comparative analysis. Both the 2D and the hydrogen bond surface representations at the metal complex/drug-receptor interaction site have been shown in Figure 9. Furthermore, further information on the binding interactions has been tabulated in Tables 5 and 15S. The results showed that while the H₂BT ligand and Co²⁺ complex showed lower binding energies, the potential binding energy of the Ni²⁺ and Cu²⁺ metal complexes was higher than that of the original DRO ligand.

With a docking score of -6.89 kcal/mol, the Cu²⁺ complex showed the highest affinity for binding to the 2w3l target among the four examined isolated compounds. In contrast to the DRO ligand, this implies a stronger binding. As seen in Figure 9, the Cu²⁺ complex displayed interactions in which the residues GLU73, ALA108, MET74, and PHE71 participated in π-Alkyl, π-Sigma, π-Donor Hydrogen bond, and Amide-π stacking interactions. Similarly, a theoretical binding energy of -5.51 kcal/mol was obtained by docking the Ni²⁺ complex with the 2w3l target. The interaction between the Ni²⁺ complex and 2w3l is depicted in Figure 9, emphasizing residues ALA108, MET74, and GLU73. Additionally shown is the H₂BT ligand's binding mode inside the pocket, which results in a molecular docking score of -4.07 kcal/mol. π-alkyl interactions with the MET74, ARG105, and ALA108 residues as well as a π-π T-shaped interaction with the PHE63 residue are involved in this interaction. With a docking score of -4.11 kcal/mol, the Co²⁺ complex interacts with ASP70 via a traditional hydrogen bond and with the residues VAL92, LEU96, and ALA108 through three π-alkyl interactions.

3.14.1. Docking validation

To evaluate the efficacy of the docking procedure, re-docking was conducted using a similar process, as shown in Figure 10. The 3D molecular interactions of the co-crystallized complex with the BCL2 protein (PDB ID: 2w3l) matched the 3D chemical contacts of the re-docked inhibitor with the same cell line. In comparison to both the original and re-docked complexes, the re-docked inhibitor scored -5.32 kcal/mol and displayed an Root mean square deviation (RMSD) of 0.9364 Å.

3.15. In silico pharmacokinetics analysis

It is crucial to evaluate the pharmacokinetic properties of any molecule being considered as a possible pharmacological agent before conducting *in vivo* experiments. Absorption, distribution, metabolism, excretion, and toxicity (ADME) variables are all included in this assessment. By analyzing the ADME properties of the examined compounds, the SwissADME server (<http://www.swissadme.ch/>), which follows Lipinski's rule of five, may predict the drug-likeness of those compounds. According to Lipinski's rule, typical drug-like compounds have a molecular weight of 500 Da or fewer, a Log P magnitude of 5 or less, and no more than 10 hydrogen bond donors and 5 hydrogen bond acceptors [68]. Compounds that violate certain requirements may have problems with bioavailability. But according to the ADME analysis, none of the substances went against Lipinski's rule of five.

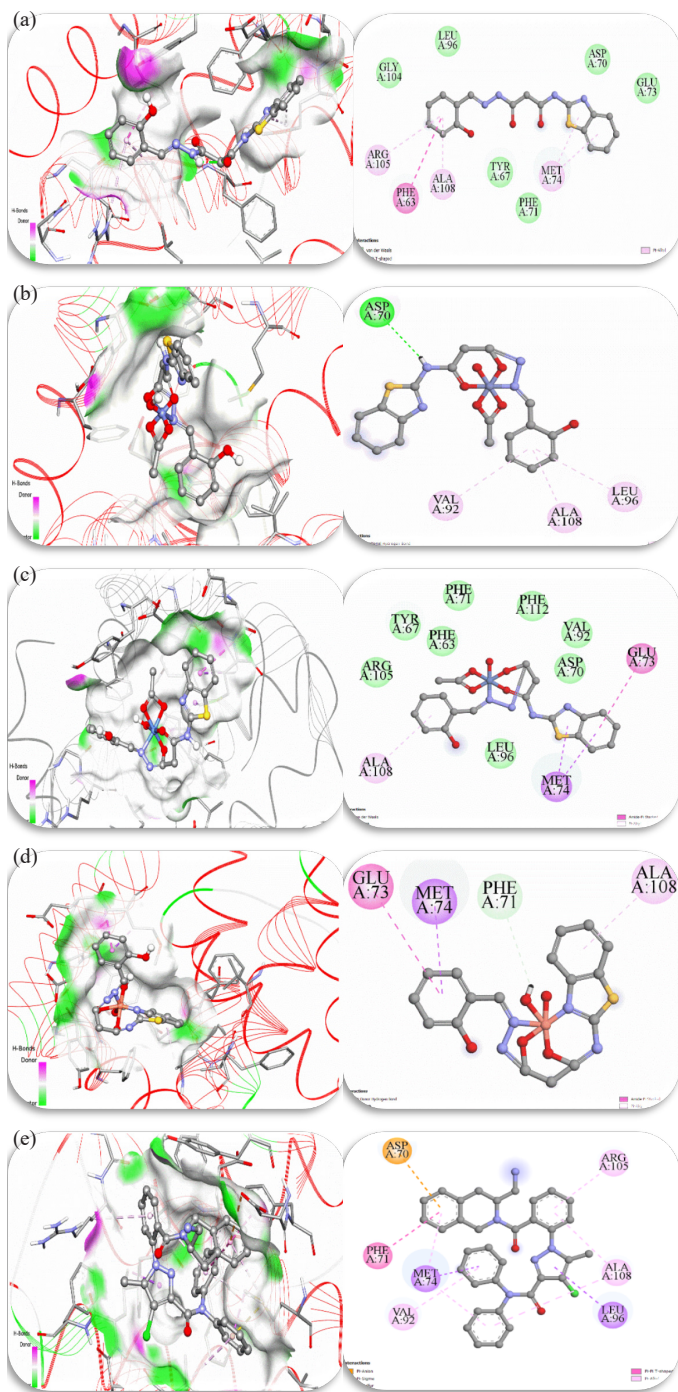


Figure 9. Interactions between the 2w3l target and the (a) H₂BT ligand, (b) Co²⁺ complex, (c) Ni²⁺ complex, (d) Cu²⁺ complex, and (e) DRO ligand in two and three dimensions (the acceptor area of the hydrogen bond surface is represented by green, and the donor area of the amino acid residues by pink).

Table 5. The most stable docking conformations are projected to have important thermodynamic characteristics.

Compound	ΔG_{bind} Free energy of binding	ΔG_{inter} Final inter-molecular energy	$\Delta G_{\text{vdw+hbond+desolv}}$ Unbound system's energy	ΔG_{elec} Electrostatic energy	ΔG_{tor} Torsional free energy
1	-4.08	-5.57	-5.52	-0.05	1.49
2	-6.89	-8.26	-8.19	-0.07	+1.37
3	-4.11	-5.90	-5.81	-0.08	+1.79
4	-5.51	-6.88	-6.84	-0.05	+1.37
DRO ligand	-5.32	-7.11	-7.18	+0.07	+1.79

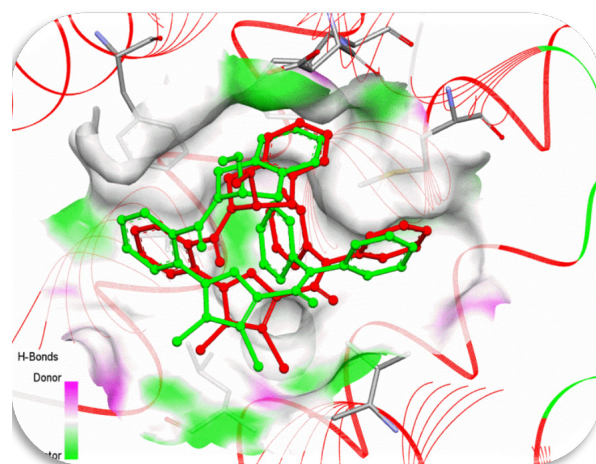


Figure 10. Co-crystalline ligand (green) and red locked ligand (red) hydrogen bond surfaces with (2w3l) DNA Helix (RMSD = 0.9364 Å).

Table 6. Using the Lipinski rule, in silico physicochemical data for drug likeness.

Properties	1	2	3	4
M.wt (g/mol)	354.38	451.94	489.37	489.13
Rotatable bonds	7	1	3	3
H-B acceptor	5	7	8	8
H-B donor	3	3	3	3
Lipinski violations	0	0	0	0
BBB	No	No	No	No
GI	High	High	Low	Low
Log S	-4.01	-4.83	-5.09	-5.09
Log Po/w	1.64	0.00	0.00	0.00
Log Kp (cm/s)	-6.22	-6.96	-6.97	-6.97
TPSA (Å ²)	131.92	127.40	159.94	159.94
Bioavailability score	0.55	0.55	0.55	0.55

BBB: The blood-brain barrier, TPSA: Topological polar surface area

The pharmacokinetic properties of synthesized drugs are presented in Table 6. All of the molecules under investigation fell below the 500 threshold, with molecular weights ranging from 354 to 489. This suggests that, in contrast to larger molecules, these chemicals are likely to be more easily absorbed, transported, and disseminated. Furthermore, it was found that the tested compounds' hydrogen bond acceptor and donor counts fell within the bounds established by Lipinski's rule. The range of hydrogen bond donors was 3 (<5), and the range of hydrogen bond acceptors was 5 to 8 (<10). There were seven rotatable bonds in the H₂BT ligand, three in the Co²⁺ and Ni²⁺ complexes, and one in the Cu²⁺ complex (<10). By analyzing six physicochemical characteristics lipophilicity, solubility, size, flexibility, polarity, and saturation the bioavailability radar rapidly determines a compound's drug-likeness. A molecule's radar plot has to fall completely into a specified physicochemical range on each axis, denoted by a pink area, in order to be classified as drug-like. Lipophilicity (-0.7 – +5.0), size (150 – 500 g/mol), polarity (20-120 Å²), solubility (Log S ≤ 6), saturation (≥ 0.25), and flexibility (≤ 9 rotatable bonds) are all within the ideal ranges shown by the pink area. Because of their strong polarity (TPSA: 127-159 Å²), all the compounds were inappropriate for oral delivery, as seen in Figure 11S.

3.16. Structure activity relationship

SAR studies often focus on linking the theoretical insights derived from density functional theory (DFT) to the biological activity

observed in the compounds under examination. Specific molecular parameters, including band gap energy (E_{gap}), chemical potential (μ), and electronegativity (χ), are relevant to both the stability and chemical reactivity of these isolated compounds. Generally, compounds that exhibit a low E_{gap} alongside high μ and χ are considered effective electron donors. The ABTS assay highlights the reactivity of these compounds, identifying the most effective antioxidants based on their reactivity. Results from the ABTS assay indicated that the Co^{2+} complex exhibited the highest antioxidant activity, likely due to its low E_{gap} , along with high μ and χ values.

Additionally, the dipole moment provided valuable insights into the biological activity of the synthesized compounds. A larger dipole moment suggests a stronger interaction with and greater affinity for the receptor amino acids in microbial protein envelopes. Antimicrobial tests identified Ni^{2+} as the most potent compound against microbes, attributed to its high dipole moment of 12.581 De. Molecular electrostatic potentials (MEPs) obtained through DFT are instrumental in predicting reactive sites within the optimized structures of the compounds studied. Variations in chemical potential are visually represented by a color gradient, blue (lowest) to red (highest), with green indicating zero potential. In this context, the red zone indicated areas prone to electrophilic attack, while the blue zone signified regions favoring nucleophilic attack. MEP studies are typically linked with cytotoxicity assessments, wherein compounds with significant negative potential areas are often deemed more toxic. Cytotoxicity assays demonstrated that the ligand (H_2BT) was the most toxic towards carcinogenic cells, supporting these findings. The docking results, alongside theoretical analyses, corroborated the cytotoxicity outcomes, suggesting that both the ligand and its Ni^{2+} complex could serve as effective anticancer agents [69].

4. Conclusions

The ball milling technology was used to manufacture the metal chelates as a green chemical strategy. All the compounds that were described using a variety of spectral analytical techniques, such as $^1\text{H}/^{13}\text{C}$ NMR, FT-IR, UV-vis, ESR, EDX, SEM, XRD, and MS. Additionally, the stages of thermal breakdown were investigated using (TG, DTG) curves which indicated the thermal stability of isolated solid chelates. The DFT theory, which has also been used to predict the E_{HOMO} , E_{LUMO} , and E_{gap} , was used to estimate the molecular modeling of all produced compounds. The results demonstrated that the ligand forms an octahedral, tri-dentate/tetra-dentate structure around the metal ions. The moderate biological activity of the substances under investigation was also validated by variable biological assays. The differences seen, especially the prominence of the Ni^{2+} complex, indicate regions ready for investigation, even though the activity caused by H_2BT and its metal chelates was found to be moderately efficient against bacterial and fungal strains. Additionally, the ligand (H_2BT) and the standard ascorbic acid showed roughly similar values in the ABTS colorimetric assay, while all the tested complexes had lower antioxidant values by compared with the standard ascorbic acid (88.5%) and the ligand (H_2BT) (85.7%). In contrast, the Co^{2+} complex had the highest value of any tested compound with an activity index of 40.6%. The impact of H_2BT on the redox behavior of a copper (II) solution was demonstrated by cyclic voltammetry, which showed variations in electrochemical data (D, E, i_p , q_{an} , q_{cs} , and Q). In contrast, the achieved current peaks have dropped as the concentration of H_2BT has increased, favoring the covalency between H_2BT and the copper ions. Additionally, there has been a shift in the anodic and cathodic potential peaks, suggesting substantial physical contact between H_2BT and copper (II).

CRedit authorship contribution statement

Khlood Abou-Melha: Data duration, formal analysis, methodology, and software; Investigation and writing – review & editing; formal analysis, investigation, writing-original draft.

Declaration of generative AI and AI-assisted technologies in the writing process

The authors confirm that there was no use of artificial intelligence (AI)-assisted technology for assisting in the writing or editing of the manuscript and no images were manipulated using AI.

Acknowledgment

The author extends its appreciation to the Deanship of Scientific Research at King Khalid University for funding this work through small group Research Project under grant number: RGP1/22/45.

Supplementary data

Supplementary material to this article can be found online at https://dx.doi.org/10.25259/AJC_56_2025.

References

- Zafar, W., Sumrra, S.H., Hassan, A.U., Chohan, Z.H., 2023. A review on 'sulfonamides': Their chemistry and pharmacological potentials for designing therapeutic drugs in medical science. *Journal of Coordination Chemistry*, **76**, 546-580. <https://doi.org/10.1080/00958972.2023.2208260>
- Zafar, W., Ashfaq, M., Sumrra, S.H., 2023. A review on the antimicrobial assessment of triazole-azomethine functionalized frameworks incorporating transition metals. *Journal of Molecular Structure*, **1288**, 135744. <https://doi.org/10.1016/j.molstruc.2023.135744>
- H. Sumrra, S., Anees, M., Asif, A., N. Zafar, M., Mahmood, K., F. Nazar, M., Khalid, M., A. Nadeem, M., U. Khan, M., 2020. Synthesis, structural, spectral and biological evaluation of metals endowed 1,2,4-triazole. *Bulletin of the Chemical Society of Ethiopia*, **34**, 335-351. <https://doi.org/10.4314/bcse.v34i2.11>
- Ritter, E., Przybylski, P., Brzezinski, B., Bartl, F., 2009. Schiff bases in biological systems. *Current Organic Chemistry*, **13**, 241-9. <https://doi.org/10.2174/138527209787314805>
- Abdel-Kader, N.S., Moustafa, H., El-Ansary, A.L., Sherif, O.E., Farghaly, A.M.A., 2021. A coumarin schiff base and its Ag(I) and Cu(II) complexes: Synthesis, characterization, DFT calculations and biological applications. *New Journal of Chemistry*, **45**, 7714-7730. <https://doi.org/10.1021/acsomega.2c07592>
- Deswal, Y., Asija, S., Kumar, D., Jindal, D.K., Chandan, G., Panwar, V., Saroya, S., Kumar, N., 2022. Transition metal complexes of triazole-based bioactive ligands: Synthesis, spectral characterization, antimicrobial, anticancer and molecular docking studies. *Research on Chemical Intermediates*, **48**, 703-729. <https://doi.org/10.1007/s11164-021-04621-5>
- Rosas-Ortiz, A., Pioquinto-Mendoza, J.R., González-Sebastián, L., Hernandez-Ortega, S., Flores-Alamo, M., Morales-Morales, D., 2021. Schiff bases as inspirational motif for the production of Ni(II) and Pd(II) coordination and novel non-symmetric Ni(II)-POCOP pincer complexes. *European Journal of Inorganic Chemistry*, **2021**, 2452-2463. <https://doi.org/10.1002/ejic.202100146>
- Lal Singh, H., Kulhari, P., Choudhary, G., Khaturia, S., 2024. Synthesis, spectral, DFT, and antibacterial studies of nickel(II) and cobalt(II) complexes with aminoantipyrine based schiff base ligands. *Inorganic Chemistry Communications*, **162**, 112192. <https://doi.org/10.1016/j.inoche.2024.112192>
- Ibrahim, K.M., Zaky, R.R., Gomaa EA, Abd El-Hady, M.N., 2023. Physicochemical studies and biological evaluation on (E)-3-(2-(1-(2-hydroxyphenyl)hydrazinyl)-3-oxo-N-(thiazol-2-yl)propanamide) complexes. *Spectrochim Acta A*, **107**, 133-144. <https://doi.org/10.1155/2012/534617>
- Suvarapu, L.N., Seo, Y.K., Baek, S.-O., Ammireddy, V.R., 2012. Review on analytical and biological applications of hydrazones and their metal complexes. *Journal of Chemistry*, **9**, 1288-1304. <https://doi.org/10.1155/2012/534617>
- Zaky, R.R., Ibrahim, K.M., Abou El-Nadar, H.M., Abo-Zeid, S.M., 2015. Bivalent transition metal complexes of (E)-3-(2-benzylidenehydrazinyl)-3-oxo-N-(p-tolyl)propanamide: Spectroscopic, computational, biological activity studies. *Spectrochimica Acta. Part A, Molecular and Biomolecular Spectroscopy*, **150**, 40-53. <https://doi.org/10.1016/j.saa.2015.04.107>
- Anacona, J.R., Noriega, N., Camus, J., 2015. Synthesis, characterization and antibacterial activity of a tridentate schiff base derived from cephalothin and sulfadiazine, and its transition metal complexes. *Spectrochimica Acta. Part A, Molecular and Biomolecular Spectroscopy*, **137**, 16-22. <https://doi.org/10.1016/j.saa.2014.07.091>
- Al-Hazmi, G.A.A., Abou-Melha, K.S., El-Metwaly, N.M., Althagafi, I., Shaaban, F., Zaky, R., 2020. Green synthesis approach for Fe(III), Cu(II), Zn(II), and Ni(II)-Schiff base complexes: spectral, conformational, MOE docking, and biological studies. *Applied Organometallic Chemistry*, **34**, 5403. <https://doi.org/10.1002/aoc.5403>
- Alkhatib F, Hameed A, Sayqal A, Bayazeed AA, Alzahrani S, Al-Ahmed ZA, Althagafi, I., Zaky, R.R., El-Metwaly, N.M., 2020. Green synthesis and characterization of new Schiff-base complexes: Spectroscopy, conductometry, Hirshfeld properties, and biological assay enhanced by in-silico study. *Arabian Journal of Chemistry*, **13**, 6327-6340. <https://doi.org/10.1016/j.molstruc.2012.02.006>

15. Alzahrani S, Morad M, Bayazeed A, Aljohani MM, Alkhatib F, Shah R, Katouah H., Abumelha, H.M., Althagafi, I., Zaky, R.R., El-Metwaly, N.M., 2020. Ball milling approach to prepare new Cd(II) and Zn(II) complexes: characterization, crystal packing, cyclic voltammetry, and MOE-docking agreements with biological assay. *Journal of Molecular Structure*, **1218**, 128473. <https://doi.org/10.1016/j.molstruc.2020.128473>
16. Hojjati-Najafabadi, A., Davar, F., Enteshari, Z., Hosseini-Koupaei, M., 2021. Antibacterial and photocatalytic behavior of green synthesis of Zn_{0.95}Ag_{0.05}O nanoparticles using herbal medicine extract. *Ceramics International*, **47**, 31617-24. <https://doi.org/10.1016/j.ceramint.2021.08.042>
17. Alharbi, A., Alzahrani, S., Alkhatib, F., Abu Al-Ola, K., Abdulaziz Alfi, A., Zaky, R., El-Metwaly, N.M., 2021. Studies on new Schiff base complexes synthesized from d10 metal ions: Spectral, conductometric measurements, DFT and docking simulation. *Journal of Molecular Liquids*, **334**, 116148. <https://doi.org/10.1016/j.molliq.2021.116148>
18. Alaysuy, O., Abumelha, H.M., Alsoliemy, A., Alharbi, A., Alatawi, N.M., Osman, H.E.M., 2022. Elucidating new hydrazide-based complexes derived from Pd(II), Cu(II), and Cd(II) ions: studies concerning spectral, DFT, Hirshfeld-crystal, biological screening, and Swiss-ADME verification. *Journal of Molecular Structure*, **1259**, 132748. <https://doi.org/10.1016/j.molstruc.2022.132748>
19. Hassan, A.U., Sumrra, S.H., Zafar, W., Imran, M., Noreen, S., Irfan, M., 2023. Enriching the compositional tailoring of NLO responsive dyes with diversity oriented electron acceptors as visible light harvesters: A DFT/TD-DFT approach. *Molecular Physics*, **121**. <https://doi.org/10.1080/00268976.2022.2148585>
20. Hassan, A.U., Sumrra, S.H., Zubair, M., Mustafa, G., Nazar, M.F., Zafar, M.N., 2023. Structurally modulated D-π-D-A (semiconductor) anchoring dyes to enhance the tunable NLO response: a DFT/TDDFT quest for new photovoltaic materials. *Structural Chemistry*, **34**, 1043-1060. <https://doi.org/10.1016/j.saa.2007.05.034>
21. Zalaoglu, Y., Ulgen, A., Terzioglu, C., Yildirim, G., 2010. Theoretical study on the characterization of 6-methyl-1,2,3,4-tetrahydroquinoline using quantum mechanical calculation methods. *Fen Bilimleri Dergisi*, **14**, 66-76. <https://doi.org/10.1016/j.saa.2007.05.034>
22. Stylianakis, I., Kolocouris, A., Kolocouris, N., Fytas, G., Foscolos, G.B., Padalko, E., Neyts, J., De Clercq, E., 2003. Spiro[pyrrolidine-2,2'-adamantanes]: Synthesis, anti-influenza virus activity, and conformational properties. *Bioorganic & Medicinal Chemistry Letters*, **13**, 1699-1703. [https://doi.org/10.1016/s0960-894x\(03\)00231-2](https://doi.org/10.1016/s0960-894x(03)00231-2)
23. Singh, H.L., Khaturia, S., Solanki, V.S., Sharma, N., 2023. Synthesis of coordination compounds of dibutyltin(IV) with Schiff bases having nitrogen donor atoms. *Journal of the Indian Chemical Society*, **100**, 100945. <https://doi.org/10.1016/j.jics.2023.100945>
24. Mansoorianfar, M., Shahin, K., Hojjati-Najafabadi, A., Pei, R., 2022. MXene-laden bacteriophage: A new antibacterial candidate to control bacterial contamination in water. *Chemosphere*, **290**, 133383. <https://doi.org/10.1016/j.chemosphere.2021.133383>
25. Ahamed, A., Arif, I.A., Mateen, M., Surendra Kumar, R., Idhayadhulla, A., 2018. Antimicrobial, anticoagulant, and cytotoxic evaluation of multidrug resistance of new 1,4-dihydropyridine derivatives. *Saudi Journal of Biological Sciences*, **25**, 1227-1235. <https://doi.org/10.1016/j.sjbs.2018.03.001>
26. Hassan, G.S., El-Messery, S.M., Abbas, A., 2017. Synthesis and anticancer activity of new thiazolo[3,2-a]pyrimidines: DNA binding and molecular modeling study. *Bioorganic Chemistry*, **74**, 41-52. <https://doi.org/10.1016/j.bioorg.2017.07.008>
27. Denizot, F., Cois, Lang, R., 1986. Rapid colorimetric assay for cell growth and survival. *Journal of Immunological Methods*, **89**, 271-7. [https://doi.org/10.1016/0022-1759\(86\)90368-6](https://doi.org/10.1016/0022-1759(86)90368-6)
28. Mitra, I., Mukherjee, S., Reddy, V.P., Dasgupta, S., Bose, J.C., Mukherjee, S., Linert, W., Moi, S.C., 2016. Benzimidazole based Pt(II) complexes with better normal cell viability than cisplatin: synthesis, substitution behavior, cytotoxicity, DNA binding and DFT study. *RSC Advances*, **6**, 76600-76613. <https://doi.org/10.1039/C6RA17788C>
29. Aliaga, C., Lissi, E.A., 1998. Reaction of 2,2'-azinobis 3-ethylbenzothiazoline-6-sulfonic acid (ABTS) derived radicals with hydroperoxides: kinetics and mechanism. *International Journal of Chemical Kinetics*, **30**, 565-570. [https://doi.org/10.1002/\(SICI\)1097-4601\(1998\)30:8<565::AID-KIN5>3.0.CO;2-Q](https://doi.org/10.1002/(SICI)1097-4601(1998)30:8<565::AID-KIN5>3.0.CO;2-Q)
30. C, S., S, D.K., Raganathan, V., Tiwari, P., A, S., P, B.D., 2022. Molecular docking, validation, dynamics simulations, and pharmacokinetic prediction of natural compounds against the SARS-coV-2 main-protease. *Journal of Biomolecular Structure & Dynamics*, **40**, 585-611. <https://doi.org/10.1080/07391102.2020.1815584>
31. Valdés-Tresanco, M.S., Valdés-Tresanco, M.E., Valiente, P.A., Moreno, E., 2020. AMDock: A versatile graphical tool for assisting molecular docking with autodock vina and Autodock4. *Biology Direct*, **15**, 12. <https://doi.org/10.1186/s13062-020-00267-2>
32. Porter, J., Payne, A., de Candole, B., Ford, D., Hutchinson, B., Trevitt, G., Turner, J., Edwards, C., Watkins, C., Whitcombe, I., Davis, J., Stubberfield, C., 2009. Tetrahydroisoquinoline amide substituted phenyl pyrazoles as selective bcl-2 inhibitors. *Bioorganic & Medicinal Chemistry Letters*, **19**, 230-3. <https://doi.org/10.1016/j.bmcl.2008.10.113>
33. Younis, A.M., Rakha, T.H., El Gamil, M.M., Abu El Reash, G.M., 2022. Synthesis and characterization of some complexes derived from isatin dye ligand and study of their biological potency and anticorrosive behavior on aluminum metal in acidic medium. *Journal of Inorganic and Organometallic Polymers and Materials*, **32**, 895-911.
34. Adam, F.A., Abou El-Reash, Y.G., Ghoniem, M.G., Zaky, R.R., 2024. Investigate the effect of SiO₂ on the chelation behavior of benzothiazole derivatives towards Ni(II), Co(II), and Cu(II) metal ions: Quantitative structure, cyclic voltammetry and biological activity relationships. *Silicon*, **16**, 2415-2439. <https://doi.org/10.1007/s12633-023-02843-3>
35. Abdel-Rhman, M.H., El-Asmy, A.A., Ibrahim, R., Hosny, N.M., 2023. New Schiff base ligand and some of its coordination compounds: Synthesis, spectral, molecular modeling and biological studies. *Journal of Molecular Structure*, **1279**, 135023. <https://doi.org/10.1016/j.molstruc.2023.135023>
36. Abdel-Rhman, M.H., Motawea, R., Belal, A., Hosny, N.M., 2022. Spectral, structural and cytotoxicity studies on the newly synthesized n',n'-diisonicotinoylmalonohydrazide and some of its bivalent metal complexes. *Journal of Molecular Structure*, **1251**, 131960. <https://doi.org/10.1016/j.molstruc.2021.131960>
37. Hosny, N., Ibrahim, R., El-Asmy, A., 2016. Spectral, thermal, optical and biological studies on (E)-4-[(2-hydroxyphenyl)imino]pentan-2-one and its complexes. *Journal of the Serbian Chemical Society*, **81**, 57-66. <https://doi.org/10.2298/jsc150201058h>
38. Nageeb, A.S., Morsi, M.A., Gomaa, E.A., Hammouda, M.M., Zaky, R.R., 2024. Comparison on biological inspection, optimization, cyclic voltammetry, and molecular docking evaluation of novel bivalent transition metal chelates of Schiff base pincer ligand. *Journal of Molecular Structure*, **1300**, 137281. <https://doi.org/10.1016/j.molstruc.2023.137281>
39. Alsulami, Q.A., Rajeh, A., Mannaa, M.A., Albukhari, S.M., Baamer, D.F., 2021. Preparation of highHBTy efficient sunlight driven photodegradation of some organic pollutants and H₂ evolution over rGO/FeVO₄ nanocomposites. *International Journal of Hydrogen Energy*, **46**, 27349-27363. <https://doi.org/10.1016/j.ijhydene.2021.05.211>
40. Hathaway, B.J., Billing, D.E., 1970. The electronic properties and stereochemistry of mono-nuclear complexes of the copper(II) ion. *Coordination Chemistry Reviews*, **5**, 143-207. [https://doi.org/10.1016/s0010-8545\(00\)80135-6](https://doi.org/10.1016/s0010-8545(00)80135-6)
41. Abdel-Rhman, M.H., Samir, G., Hussien, M.A., Hosny, N.M., 2024. Transition metal complexes of n'-(2-cyanoacetyl)nicotinohydrazide: Synthesis, structural and anticancer activity studies. *Polyhedron*, **247**, 116709. <https://doi.org/10.1016/j.poly.2023.116709>
42. Hosny, N.M., Ibrahim, O.A., Belal, A., Hussien, M.A., Abdel-Rhman, M.H., 2023. Synthesis, characterization, DFT, cytotoxicity evaluation and molecular docking of a new carbothioamide ligand and its coordination compounds. *Results in Chemistry*, **5**, 100776. <https://doi.org/10.1016/j.rchem.2023.100776>
43. Adam, F.A., Abou El-Reash, Y.G., Ghoniem, M.G., Zaky, R.R., 2024. Green processing and characterization of novel HETERO-ligand co(II) complexes with cyanopyridine derivatives: Quantitative structure, computational assessment, and biological activity relationship. *Journal of Molecular Structure*, **1308**, 137947. <https://doi.org/10.1016/j.molstruc.2024.137947>
44. Manimohan, M., Pugalmani, S., Sithique, M.A., 2020. Biologically active water-soluble novel biopolymer/hydrazide-based O-carboxymethyl chitosan Schiff bases: Synthesis and characterization. *Journal of Inorganic and Organometallic Polymers and Materials*, **30**, 3658-3676.
45. Hassan, S.M., Ahmed, A.I., Mannaa, M.A., 2018. Structural, photocatalytic, biological and catalytic properties of SnO₂/TiO₂ nanoparticles. *Ceramics International*, **44**, 6201-6211.
46. Wang, S., Yu, J., Yu, J., 2008. Conformation and location of amorphous and semi-crystalline regions in c-type starch granules revealed by SEM, NMR and XRD. *Food Chemistry*, **110**, 39-46. <https://doi.org/10.1016/j.foodchem.2008.01.052>
47. Hajji, M., Amiri, N., Ben Taheur, F., Bujacz, A., Nasri, H., Guerfel, T., 2020. Heteroleptic cobalt(II) complex with nitrogen-rich macrocycles structure, bioactivity and DFT modelling. *Solid State Sciences*, **100**, 106117. <https://doi.org/10.1016/j.foodchem.2008.01.052>
48. Avci, D., Altürk, S., Sönmez, F., Tamer, Ö., Başoğlu, A., Atalay, Y., Zengin Kurt B, Dege N., 2018. Three novel Cu(II), Cd(II), and Cr(III) complexes of 6-methylpyridine-2-carboxylic acid with thiocyanate: synthesis, crystal structures, DFT calculations, molecular docking and α-glucosidase inhibition studies. *Tetrahedron*, **74**, 7198-7208. <https://doi.org/10.1016/j.tet.2020.106117>
49. da Silva, R.R., Ramalho, T.C., Santos, J.M., Figueroa-Villar, J.D., 2006. On the limits of highest-occupied molecular orbital driven reactions: The frontier effective-for-reaction molecular orbital concept. *The Journal of Physical Chemistry A*, **110**, 1031-1040. <https://doi.org/10.1021/jp054434y>
50. Zaky, R., Fekri, A., 2015. Structural, spectral and DFT studies of N-ethyl-2-(4-(phenylamino)-4-thioxobutan-2-ylidene)hydrazinecarbothioamide complexes synthesized by ball milling. *Journal of Molecular Structure*, **1079**, 203-213. <https://doi.org/10.1016/j.molstruc.2014.09.033>
51. Khan, A.S.A., Ahmed, R., Mirza, M.L., 2010. Evaluation of kinetic parameters of uranyl acetate complexes in ethanolic solution by cyclic voltammetry. *Journal of Radioanalytical and Nuclear Chemistry*, **283**, 527-531. <https://doi.org/10.1007/s10967-009-0372-4>
52. Gomaa, E.A., 2012. Solubility and solvation parameters of barium sulfate in mixed ethanol-water mixtures at 301.15 K. *International Journal of Materials and Chemistry*, **2**, 16-8. <https://doi.org/10.1007/s10967-009-0372-4>
53. Garcia-Miranda Ferrari, A., Foster, C.W., Kelly, P.J., Brownson, D.A.C., Banks, C.E., 2018. Determination of the electrochemical area of screen-printed electrochemical sensing platforms. *Biosensors*, **8**, 53. <https://doi.org/10.3390/bios8020053>
54. El-Shereafy, S.E., Gomaa, E.A., Yousef, A.M., Abou El-Yazed, A.S., 2017. Electrochemical and thermodynamic estimations of the interaction parameters for bulk and nano-silver nitrate (NSN) with cefdinir drug using a glassy carbon electrode. *Iranian Journal of Materials Science and Engineering*, **14**, 48-57. <https://doi.org/10.3390/bios8020053>
55. Zhao, K., Song, H., Zhuang, S., Dai, L., He, P., Fang, Y., 2007. Determination of nitrite with the electrocatalytic property to the oxidation of nitrite on thionine modified aligned carbon nanotubes. *Electrochemistry Communications*, **9**, 65-70. <https://doi.org/10.1016/j.elecom.2006.07.001>
56. Brownson, D.A.C., Banks, C.E., 2024. *The Handbook of Graphene Electrochemistry*. 2014.
57. Shaikh, A.A., Begum, M., Khan, A.H., Ehsan, M.Q., 2006. Cyclic voltammetric studies of the redox behavior of iron(III)-vitamin B6 complex at carbon paste

- electrode. *Russian Journal of Electrochemistry*, **42**, 620-5. <https://doi.org/10.1134/S1023193506060048>
58. Karrouchi, K., Radi, S., Ramli, Y., Taoufik, J., Mabkhot, Y.N., Al-aizari, F.A., Ansar, M., 2018. Synthesis and pharmacological activities of pyrazole derivatives: A review. *Molecules*, **23**, 134. <https://doi.org/10.1134/S1023193506060048>
59. Murugaiyan, M., Mani, S.P., Sithique, M.A., 2019. Zinc(II)-centered biologically active novel N,N,O donor tridentate water-soluble hydrazide-based O-carboxymethyl chitosan Schiff base metal complexes: synthesis and characterization. *New Journal of Chemistry*, **43**, 15590-15600. <https://doi.org/10.3390/molecules23010134>
60. Metwally, M.A., Gouda, M.A., Harmal, A.N., Khalil, A.M., 2012. Synthesis, antitumor, cytotoxic and antioxidant evaluation of some new pyrazolotriazines attached to antipyrine moiety. *European Journal of Medicinal Chemistry*, **56**, 254-262. <https://doi.org/10.1016/j.ejmech.2012.08.034>
61. M. Rabie, A., S. Tantawy, A., M. I. Badr, S., 2016. Design, synthesis, and biological evaluation of novel 5-substituted-2-(3,4,5-trihydroxyphenyl)-1,3,4-oxadiazoles as potent antioxidants. *American Journal of Organic Chemistry*, **6**, 54-80. <https://doi.org/10.5923/j.ajoc.20160602.02>
62. Mira, A., Gimenez, E.M., Bolzán, A.D., Bianchi, M.S., López-Larraz, D.M., 2013. Effect of thiol compounds on bleomycin-induced DNA and chromosome damage in human cells. *Archives of Environmental & Occupational Health*, **68**, 107-116. <https://doi.org/10.1080/19338244.2012.658120>
63. Wang, Q., Cui, K., Espin-García, O., Cheng, D., Qiu, X., Chen, Z., Moore, M., Bristow, R.G., Xu, W., Der, S., Liu, G., 2013. Resistance to bleomycin in cancer cell lines is characterized by prolonged doubling time, reduced DNA damage and evasion of G2/M arrest and apoptosis. *PloS one*, **8**, e82363. <https://doi.org/10.1371/journal.pone.0082363>
64. Loso, M.R., Benko, Z., Buysse, A., Johnson, T.C., Nugent, B.M., Rogers, R.B., Sparks, T.C., Wang, N.X., Watson, G.B., Zhu, Y., 2016. SAR studies directed toward the pyridine moiety of the sap-feeding insecticide sulfoxaflor (Isoclast™ active), *Bioorganic & Medicinal Chemistry*, **24**, 378-82. <https://doi.org/10.1371/journal.pone.0082363>
65. Khedr, A.K., Zaky, R.R., Gomaa, E.A., El-hady, M.N.A., 2022. Elucidation for coordination features of N-(benzothiazol-2-yl)-3-oxo-3-Structural description, DFT geometry optimization, cyclic voltammetry and biological inspection. *Journal of Molecular Liquids*, **368**, 120613. <https://doi.org/10.1016/j.bmc.2015.11.022>
66. Tessoulin, B., Papin, A., Gomez-Bougie, P., Bellanger, C., Amiot, M., Pellat-Deceunynck, C., Chiron, D., 2019. BCL2-family dysregulation in b-cell malignancies: From gene expression regulation to a targeted therapy biomarker. *Frontiers in Oncology*, **8**, 645. <https://doi.org/10.3389/fonc.2018.00645>
67. Youle, R.J., Strasser, A., 2008. The BCL-2 protein family: Opposing activities that mediate cell death. *Nature Reviews. Molecular Cell Biology*, **9**, 47-59. <https://doi.org/10.1038/nrm2308>
68. Lipinski, C.A., Lombardo, F., Dominy, B.W., Feeney, P.J., 2012. Experimental and computational approaches to estimate solubility and permeability in drug discovery and development settings. *Advanced Drug Delivery Reviews*, **64**, 4-17. <https://doi.org/10.1016/j.addr.2012.09.019>
69. Singh, H.L., Dhingra, N., Bhanuka, S., 2023. Synthesis, spectral, antibacterial and QSAR studies of tin and silicon complexes with schiff base of amino acids. *Journal of Molecular Structure*, **1287**, 135670. <https://doi.org/10.1016/j.molstruc.2023.135670>